

# NUMERICAL INVESTIGATION OF THE INTERACTION BETWEEN LOCAL FLOW STRUCTURES AND PARTICULATE FOULING ON STRUCTURED HEAT TRANSFER SURFACES

Robert Kasper, Johann Turnow and Nikolai Kornev

Chair of Modeling and Simulation

Department of Mechanical Engineering and Marine Technology, University of Rostock  
Albert-Einstein-Str. 2, 18059 Rostock, Germany  
robert.kasper@uni-rostock.de

## ABSTRACT

A novel large-scale resolving multiphase method for the numerical simulation of particulate fouling is applied to structured heat transfer surfaces, which is based on a coupling of the Lagrangian-Particle-Tracking (LPT) and Eulerian approach. Hence, suspended particles are simulated according to their natural behavior by means of LPT as solid spherical particles whereas the carrier phase is simulated using the Eulerian approach. Large Eddy Simulations (LES) are performed for turbulent channel flows at  $Re_\tau = 395$  combined with two kinds of surface structures (square cavity and spherical dimple) and foulant particle mass loading ratios up to  $\beta = \dot{m}_p/\dot{m}_f = 0.002$  using a dynamic one equation eddy-viscosity turbulence model. These simulations demonstrate the great capabilities of the proposed method to analyze the interaction between local flow structures and different fouling mechanisms (e.g. formation and removal of fouling deposits) in a comprehensive way. Furthermore, the conducted computations reveals a slightly better fouling performance and thermo-hydraulic efficiency of the spherical dimple due to the existence of asymmetric vortex structures compared to the square cavity.

## INTRODUCTION

Particulate fouling of heat transfer surfaces due to suspended material within the heat exchanger working fluid is still one of the most important problems in heat exchangers. It has been described as the major unresolved and most challenging problem in heat transfer (Awad, 2011). Fouling increases the heat transfer resistance and reduces the effectiveness of heat exchangers which causes higher fuel consumption, maintenance costs and costs due to production loss (Müller-Steinhagen, 2010). Despite the fact that particulate fouling reduces the heat transfer and increases the pressure loss, the performance of heat transfer enhancement methods like ribs, fins or dimples is commonly characterized by the thermo-hydraulic efficiency (Gee and Webb, 1980) or number of transfer units NTU (Shah and Sekulić, 2003), which does not include any information about the fouling behavior. In addition to it, a more or less universal method for the prediction of particulate fouling does still not exist. Existing fouling models (e.g., Kern and Seaton (1969) and Taborek et al. (1972)) are derived for numerous assumptions and simplifications. Hence, existing fouling modeling approaches are unsuitable for a general prediction of particulate fouling and a detailed analysis of fundamental fouling mechanisms. Due to the steadily growing computational resources, the simulation of highly complex processes like particulate fouling using computational fluid dynamics (CFD) becomes more and more important and could be a reliable alternative to expensive experimental measurements. In contrast to several numerical investigations of heat transfer enhancement methods, e.g. Elyyan et al. (2008) and Turnow et al. (2011), CFD studies of structured heat transfer surfaces considering particulate fouling are relatively seldom. Moreover, an extensive analysis of the in-

teraction between local flow structures and fouling deposits using transient, large-scale resolving numerical methods such as LES or hybrid URANS-LES does not exist at this moment.

The present study is aimed to fill up this lack of knowledge by introducing a new multiphase Eulerian-Lagrangian approach which is suitable for CFD studies of heat transfer enhancement methods under consideration of particulate fouling and local flow structures using large-scale resolving methods.

## NUMERICAL METHODS

The applied multiphase method is composed of two different branches which are closely related to each other. The first one is the Lagrangian branch and describes the physics of the suspended particles or respectively the foulant using the LPT. This branch is mainly responsible for the mass transport of the particles to the heat transfer surfaces, the formation of fouling deposits due to adhesion and sedimentation and also the removal of fouling deposits due to local shear forces. The second one is the Eulerian branch which determines the flow fields of the carrier flow with respect to the fouling deposits.

## LAGRANGIAN BRANCH

In order to describe the motion of isothermal, fully spherical particles within a fluid using the Lagrangian-Particle-Tracking (LPT) the solution of the following set of ordinary differential equations is required. This allows one to calculate the particle location and the linear as well as the angular particle velocity at any time:

$$\frac{d\mathbf{x}_p}{dt} = \mathbf{u}_p, \quad (1)$$

$$m_p \frac{d\mathbf{u}_p}{dt} = \sum \mathbf{F}_i, \quad (2)$$

$$I_p \frac{d\boldsymbol{\omega}_p}{dt} = \sum \mathbf{T}, \quad (3)$$

where  $m_p$  is the particle mass,  $I_p$  is the moment of inertia,  $\mathbf{F}_i$  includes all forces acting on the particle and  $\mathbf{T}$  is the torque acting on the rotating particle due to viscous interaction with the carrier fluid (Sommerfeld, 2010). Newton's second law of motion, Eq. (2), requires the consideration of all relevant forces acting (e.g. drag and gravity/buoyancy force) on the particle:

$$m_p \frac{d\mathbf{u}_p}{dt} = \sum \mathbf{F}_i = \mathbf{F}_D + \mathbf{F}_G + \dots \quad (4)$$

However, analytical representation for different forces exists only for small particle Reynolds numbers respectively for the Stokes

regime (Crow et al., 2011). Thus, the drag force is expressed more generally in terms of a drag coefficient  $C_D$ . The implemented drag model is based on the particle Reynolds number, which is defined as

$$\text{Re}_p = \frac{\rho_f D_p |\mathbf{u}_f - \mathbf{u}_p|}{\mu_f}, \quad (5)$$

with the density  $\rho_f$  and the dynamic viscosity  $\mu_f$  of the fluid or continuous phase, the particle diameter  $D_p$  and the magnitude of the relative slip velocity  $|\mathbf{u}_f - \mathbf{u}_p|$ . The drag coefficient is determined using the following drag model based on the correlation proposed by Putnam (1961):

$$C_D = \begin{cases} \frac{24}{\text{Re}_p} \left(1 + \frac{1}{6} \text{Re}_p^{2/3}\right) & \text{if } \text{Re}_p \leq 1000 \\ 0.424 & \text{if } \text{Re}_p > 1000, \end{cases} \quad (6)$$

which is suitable to higher Reynolds numbers ( $\text{Re}_p < 1000$ ) and ensures the correct limiting behavior within the Newton regime. After determination of the drag coefficient, the basic force representation is used to evaluate the drag force for a spherical particle:

$$\mathbf{F}_D = C_D \frac{\pi D_p^2}{8} \rho_f (\mathbf{u}_f - \mathbf{u}_p) |\mathbf{u}_f - \mathbf{u}_p|. \quad (7)$$

Moreover, the proposed LPT is capable to consider the most important particle forces as gravity and buoyancy, pressure gradient force, added mass force, lift forces (Saffman and Magnus) and thermophoretic forces. Four-way phase coupling is applied using a time-dependent volumetric source term within the momentum balance of the carrier fluid and a soft-sphere model (including a spring, slider and dash-pot) for the particle-particle interactions.

## Formation of fouling deposits

Due to the fact that particle deposition is mainly caused by particle-wall adhesion within this work (this assumption is applicable to particle diameters of  $D_p \leq 100 \mu\text{m}$  (Epstein, 1988)), the implemented particle deposition model is based on the suggestions of Löffler and Muhr (1972) and furthermore Heintz and Bohnet (2005). This model consists of an energy balance around the particle-wall and particle-fouling collision. Thus, a critical particle velocity can be derived according to the DLVO theory from a local energy balance which contains the kinetic energy before and after the collision, the energy ratio describing the adhesion due to London-Van der Waals forces and a specific amount considering the energy loss of a particle due to particle-wall and particle-fouling collision. From the condition of adhesion, the critical particle velocity yields:

$$u_{p,crit} = \sqrt{\left( \frac{\hbar \varpi}{e D_p 4 \pi^2 z_0^2} \right)^2 \frac{3}{4 H \rho_p}}, \quad (8)$$

where  $\hbar \varpi$  is the Lifshitz-Van der Waals energy,  $z_0$  is the distance at contact,  $H$  is the strength of the contact wall and  $e$  is the coefficient of restitution. It should be mentioned at this point, that the determination of the critical particle velocity Eq. (8) can be easily extended for the consideration of electrostatic double-layer interaction forces (Heintz, 2005). However, only London-Van der Waals forces are considered in a first step. Thus, the condition of sticking

is achieved, if the particle velocity before the wall collision (impact velocity) is smaller than the critical particle velocity ( $|\mathbf{u}_p| \leq u_{p,crit}$ ). To increase the computational efficiency of our approach, particles which fulfill the adhesion condition are converted into an additional solid phase (fouling deposits) and will be deactivated within the LPT. Thus, the amount of particles is kept nearly constant during the calculations which reduces the computational time enormously. The initiated fouling volume or fouling phase fraction  $\alpha$  is evaluated by the particle volume with respect to the cell volume:

$$\alpha_{new,i} = \alpha_{old,i} + \frac{V_p}{V_{c,i}}, \quad (9)$$

where  $\alpha_{old,i}$  is the phase fraction from the previous time step,  $V_p$  and  $V_{c,i}$  are the particle and cell volume respectively. Figure 1 shows the basic concept of the implemented phase conversion algorithm.

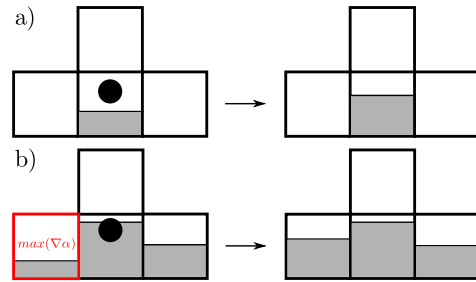


Figure 1. Basic mechanism of the phase conversion algorithm: a)  $V_c > V_p$  and b)  $V_c < V_p$

According to this, it can be distinguished between two different cases if a deposited particle has to be converted into the fouling phase. If the residual local cell volume is greater than the particle volume, the new phase fraction  $\alpha$  can be simply determined using Eq. (9). If the remaining local cell volume is smaller than the particle volume, the phase fraction is allocated to the neighbor cell with the maximum cell-based phase fraction gradient  $\max(\nabla \alpha)$ . Hence the neighbor cell with the lowest phase fraction is filled with the fouling phase. To consider the influence of the fouling phase, an additional porosity source term (based on Darcy's law)

$$\mathbf{S}_p = \alpha \frac{\mu_f}{K} \mathbf{u}_f, \quad (10)$$

has been introduced into the momentum balance equation, where  $K$  is the isotropic permeability of the fouling phase. Thus, the blocking effect or flow section contraction due to deposited particles is not explicitly considered within the calculations but rather is modeled implicitly in terms of a porous fouling layer. Furthermore any physical property  $\varphi_i$  (e.g., density, dynamic/kinematic viscosity or thermal diffusivity) for partially filled cells is interpolated as follows:

$$\varphi_i = \alpha \varphi_{fouling} + (1 - \alpha) \varphi_{fluid}, \quad (11)$$

whereas the physical properties of the carrier fluid are fully applied at cells without fouling phase ( $\alpha = 0$ ) and cells which are completely occupied by the fouling phase ( $\alpha = 1$ ) takes the physical properties of the fouling material. This procedure allows likewise

the evaluation of the heat transfer under consideration of particulate fouling and prevents the solving of an additional advection/transport equation for the fouling phase and furthermore the application of costly re-meshing procedures.

### Removal of fouling deposits

The removal or re-entrainment process of fouling deposits due to high local shear forces is an important mechanism, which has to be considered for a physical simulation of the fouling behavior. Therefore, a removal model is derived based on the suggestions of Kern and Seaton (1969) and Taborek et al. (1972):

$$\alpha_{removed} = \frac{V_p}{\tau_{rel}} \frac{|\tau_c|}{V_c}, \quad (12)$$

where  $\tau_{rel}$  is a relative shear stress and  $\tau_c$  is the cell-based local shear stress. The relative shear stress has to be measured in experiments and can be interpreted as a strength threshold value at which the removal of the fouling deposits begins. The number of particles for the re-entrainment into the carrier fluid can be determined using the definition of the sphere volume and will be reactivated within the LPT, whereby the initial momentum and forces are calculated according to the force models described above.

### EULERIAN BRANCH

The continuous phase or carrier fluid is assumed to be incompressible. Therefore, the governing equations are the incompressible Navier-Stokes equations (extended by the porosity source term  $S_p$ , which takes the influence of the fouling layer into account), the continuity equation and a passive scalar transport equation for the temperature. This system of partial differential equations is solved numerically using a 3-D finite volume method. Although the turbulence modeling is generic Large Eddy Simulations (LES) are carried out to investigate the interaction between local vortex structures and particulate fouling. LES is a widely used technique for simulating turbulent flows and allows one to explicitly solve for the large eddies and implicitly account for the small eddies by using a subgrid-scale model (SGS model).

### Large Eddy Simulation

The LES equations are derived by filtering the continuity equation, the Navier-Stokes equations and the simplified energy balance equation using an implicit filtering (mesh) with filter width  $\bar{\Delta}$ :

$$\nabla \cdot \bar{\mathbf{u}} = 0, \quad (13)$$

$$\frac{\partial \bar{\mathbf{u}}}{\partial t} + \nabla \cdot (\bar{\mathbf{u}} \bar{\mathbf{u}}) = -\frac{1}{\rho} \nabla p + \nabla \cdot \mathbf{v} \left( \nabla \bar{\mathbf{u}} + \nabla \bar{\mathbf{u}}^T \right) - \nabla \cdot \tau_{SGS} - \bar{S}_p, \quad (14)$$

$$\frac{\partial \bar{T}}{\partial t} + \nabla \cdot (\bar{\mathbf{u}} \bar{T}) = \nabla \cdot \left( \frac{\nu(\alpha)}{\text{Pr}(\alpha)} \nabla \bar{T} - \mathbf{J}_{SGS} \right). \quad (15)$$

The unclosed subgrid-scale stress tensor  $\tau_{SGS} = \bar{\mathbf{u}} \bar{\mathbf{u}} - \bar{\mathbf{u}} \bar{\mathbf{u}}$  is modeled using a dynamic one equation eddy-viscosity model proposed by Yoshizawa and Horiuti (1985) and Kim and Menon (1995). This SGS model uses a modeled balance to simulate the behavior of the subgrid-scale kinetic energy  $k_{SGS}$  in which the dynamic procedure of Germano et al. (1991) is applied to evaluate all required coefficients dynamically in space and time, while an effect of the particles on the subgrid-scales is neglected. The subgrid-scale heat flux  $\mathbf{J}_{SGS}$  is considered using a gradient-diffusion approach.

## RESULTS AND DISCUSSIONS

### Computational setup

Two academical testcases, a smooth narrow channel with a spherical dimple and a square cavity, have been chosen to investigate the fouling behavior and vortex structures of structured heat transfer surfaces by our proposed approach. The computational domain for both test cases is shown in Figure 2. The origin of the

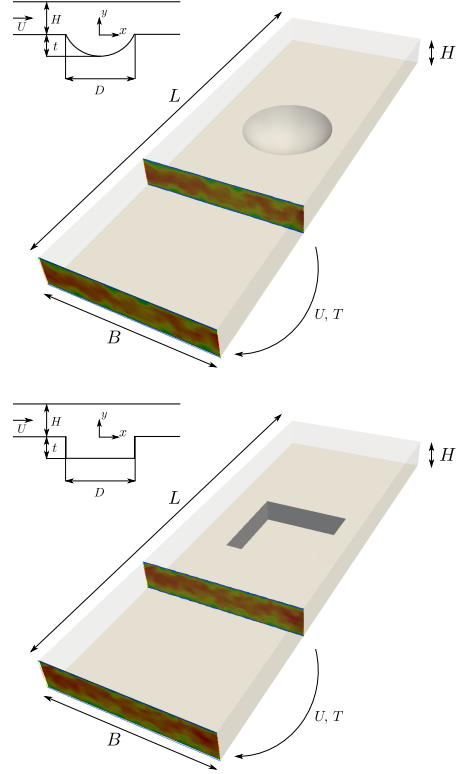


Figure 2. Computational domain for a smooth channel with a single spherical dimple (above) and a square cavity (below)

coordinate system is located in the center of the dimple respectively the cavity and is projected onto the lower wall plane, therefore the lower wall is located at  $y/H = 0.0$ . The length of the channel is  $L = 0.23$  m, while channel height  $H$  and channel width  $B$  is set to  $H = 0.015$  m and  $B = 0.08$  m. For the spherical dimple with a sharp edge a diameter of  $D = 0.046$  m and a dimple depth  $t = 0.012$  m is chosen, while the side length of the square cavity equals the dimple diameter  $D$  and the cavity depth is likewise set to  $t = 0.012$  m. Periodic boundary conditions were applied in spanwise direction, whereas no slip boundary conditions were set at the lower and upper channel walls. Turbulent inlet conditions were produced using a recycling method, which copies the turbulent velocity and temperature field from a plane downstream the channel entrance back onto the inlet. The nondimensionalized form of the temperature  $T^+ = (T - T_\infty)/(T_w - T_\infty)$  is used, where a constant  $T^+ = 1$  is assumed at the lower wall. The molecular Prandtl number  $\text{Pr}$  was set to 0.71 in all simulations, whereas the turbulent Prandtl number  $\text{Pr}_t$  is 0.9. The Reynolds number based on the averaged bulk velocity  $u_b$  and the dimple diameter or respectively the cavity side length  $D$  was equal to  $\text{Re}_D = 42000$ . To assure grid independence of the obtained results a series of calculations on different grid resolutions was carried out. Therefore block structured curvilinear grids consisting of

around  $7.8 \cdot 10^5$ ,  $1.6 \cdot 10^6$  and  $3.3 \cdot 10^6$  cells was used. In spanwise and streamwise direction an equidistant grid spacing is applied, whereas in wall-normal direction a homogeneous grid stretching is used to place the first grid node inside of the laminar sublayer at  $y^+ \approx 1$ . Spherical monodisperse silicon dioxide particles ( $\text{SiO}_2$ ) with particle diameter  $D_p = 20 \mu\text{m}$  and density  $\rho_p = 2500 \text{ kg/m}^3$  are randomly injected within the flow inlet during all fouling simulations. Based on earlier experimental fouling investigations on heat exchangers by Blöchl and Müller-Steinhagen (1990) a particle mass loading ratio of  $\beta = \dot{m}_p/\dot{m}_f = 0.001$  and  $\beta = 0.002$  is chosen to ensure an asymptotic fouling layer growth and a steady-state within a few minutes of physical real time. The estimated volume fraction of the dispersed phase is  $\alpha_d < 0.001$  which corresponds to a dilute flow and allows the negligence of particle collisions (Crow et al., 2011). Hence, only two-way coupling is considered during the simulations by applying a time-dependent volumetric source term to the momentum balance equation.

### Fully developed turbulent flow in a plane channel with and without a single spherical dimple

Numerical results for a smooth channel in combination with a single spherical dimple are validated using the experimental data published by Terekhov et al. (1997) and Turnow et al. (2011) for Reynolds number  $\text{Re}_D = 40000$ . Figure 3 shows the profile of the normalized streamwise velocity  $\langle u \rangle/u_0$  and Reynolds stress  $\langle u_{rms} \rangle/u_0$  in flow direction received from URANS ( $k-\omega$ -SST model with fine grid), LES in combination with three different grid resolutions and from LDA measurements along the  $y$ -axis at  $x/D = 0.0$  and  $z/H = 0.0$  (center of the dimple). The numerical results are obtained for Reynolds number  $\text{Re}_D = 42000$  and are normalized by the maximum velocity  $u_0$  in the center of the channel at  $y = H/2$ . A satisfactory overall agreement of calculated and measured mean velocity profiles has been obtained for all three grid resolutions and streamwise locations  $x/D$ . The mean velocity profiles from LES and URANS matches well with the measurements in the center of the channel where the maximum flow velocity occurs and even in the upper near wall region. However, slight deviations from the measured profiles can be registered for both methods and all grid resolutions inside of the spherical dimple within the distinct recirculation zone. Nevertheless, since URANS and LES results are in good agreement in this region, the likeliest reason for the discrepancy between measurements and calculations might be LDA measurement problems in close proximity of the wall (Turnow, 2011). From the mean velocity profiles one can observe, that the strongest velocity gradients arises at the level of lower channel wall ( $y/H = 0.0$ ). The instabilities of the shear layer within this region results into strong vortices and therefore in high Reynolds stresses, which can be observed in all Reynolds stress profiles. Unlike the mean velocity profiles the level of the Reynolds stresses and furthermore the location of the maximum turbulent fluctuations measured in experiments can only be gained using LES. A deviation between the measured and calculated location of the maximum Reynolds stresses are notable within the center of the dimple at position  $x/D = 0.0$ . The weakness of URANS is clearly visible in the near wall region and the level of the lower wall, where the magnitude of the turbulent fluctuations can not be captured. Due to the great importance of capturing the Reynolds stresses or fluid shear forces in order to calculate a the removal rate of deposited particles, URANS seems to be inappropriate for further investigations.

Probably the most important feature of the investigated spherical dimple with a dimple depth to dimple diameter ratio of  $t/D = 0.26$  can be observed from the phase-averaged streamline pattern given in Figure 4. The streamlines shows unsteady asymmetrical vortex structures inside the dimple, which alter their orientation ar-

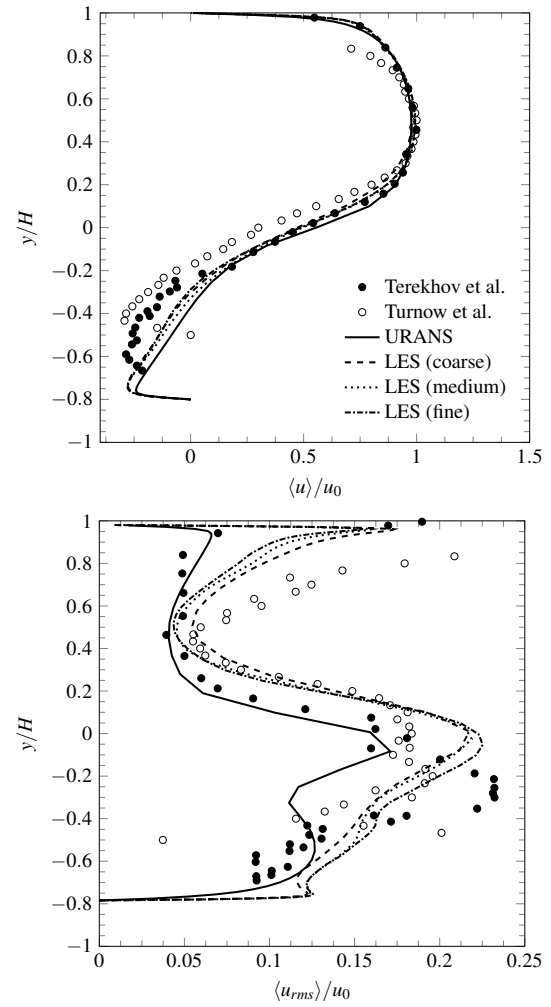


Figure 3. Normalized, time-averaged streamwise velocity and Reynolds stress profiles at  $x/D = 0.0$  and  $z/D = 0.0$  obtained from URANS and LES in comparison with experiments of Terekhov et al. (1997) and Turnow et al. (2011)

bitrary from  $-45^\circ$  to  $+45^\circ$  with respect to the main flow direction. The existence of long period self-sustained oscillations within the dimple flow could be investigated and approved as well experimentally (Terekhov, 1997) as numerically using highly resolved LES (Turnow, 2011) for dimple depth to dimple diameter ratios of  $t/D = 0.26$  and larger. In contrast to experimental observations

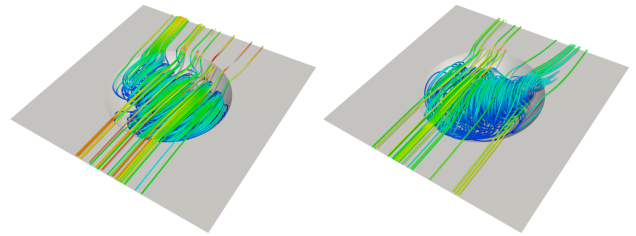


Figure 4. Different orientations ( $\pm 45^\circ$ ) of the oscillating vortex structures inside the spherical dimple for  $\text{Re}_D = 42000$

and LES results the asymmetric vortex structures obtained from URANS are steady and predicts only one of the two extreme vortex

positions ( $\pm 45^\circ$ ) in time-averaged flow pattern which are switching in reality nearly periodically. It is assumed that the self-sustained oscillations and periodically outburst due to unsteady asymmetric vortex structures enhance the wall shear stress and therefore promotes a possible self-cleaning process inside the spherical dimple and at the lower channel wall (Chudnovsky et al., 2008). Thus, LES is chosen to simulate the particulate fouling and to investigate its influence on the integral heat transfer and pressure loss.

### Particulate fouling of structured heat transfer surfaces

To investigate the influence of particulate fouling on the friction/pressure loss and heat transfer a series of LES using mass loading ratios up to  $\beta = \dot{m}_p/\dot{m}_f = 0.002$  are carried out for a single spherical dimple and a single square cavity. Due to the results given in Figure 3, a medium grid resolutions with around  $1.6 \cdot 10^6$  cells seems to be sufficient to capture as well the streamwise velocity profiles as the Reynolds stresses and is chosen for the simulation of particulate fouling. The pressure loss can be expressed in terms of the Darcy friction factor

$$f = -\frac{(dp/dx)D_h}{\rho_f u_b^2/2}, \quad (16)$$

which is directly related to the Fanning friction factor by  $C_f = f/4$ .  $(dp/dx)$  represents the pressure gradient in streamwise direction,  $D_h$  is the hydraulic diameter of the channel,  $\rho_f$  and  $u_b$  are the density and the bulk velocity of the fluid. The heat transfer is evaluated using the Nusselt number  $Nu = hL/k$ , where  $h$  is the convective heat transfer coefficient,  $L$  is a characteristic length ( $L$  is set to  $2H$  due to periodic boundary conditions in streamwise direction) and  $k$  is the thermal conductivity of the fluid. The friction coefficient  $f_0$  and Nusselt number  $Nu_0$  of the smooth channel are determined using the correlations of Petukhov and Gnielinski (Bejan and Kraus, 2003):

$$f_0 = (0.790 \ln(Re_D) - 1.64)^{-2}, \quad (17)$$

$$Nu_0 = \frac{(f_0/8)(Re_D - 1000)Pr}{1 + 12.7(f_0/8)^{1/2}(Pr^{2/3} - 1)}. \quad (18)$$

These correlations are in terms of Reynolds number based on the pipe diameter  $D$  ( $0.5 \leq Pr \leq 10^6$ ,  $2300 \leq Re_D < 5 \cdot 10^6$ ). Thus,  $Re_D$  has to be replaced by the Reynolds number based on the hydraulic diameter  $D_h = 2H$  for a smooth infinitely wide channel. The time-averaged pressure loss, integral convective heat transfer (integrated using the wall surface area from  $x/D = -0.75$  to  $x/D = 1.75$ ) and thermo-hydraulic efficiency for the clean structured surfaces with respect to the smooth channel are summarized and compared in Table 1. The evaluation of both types of structured surfaces

Table 1. Thermo-hydraulic efficiency for different (clean) structured surfaces at  $Re_D = 42000$

	$C_f/C_{f0}$	$Nu/Nu_0$	$\frac{(Nu/Nu_0)}{(C_f/C_{f0})}$	$\frac{(Nu/Nu_0)}{(C_f/C_{f0})^{1/3}}$
Cavity	1.600	1.292	0.808	1.105
Dimple	1.079	1.508	1.398	1.470

discloses the disadvantages of the square cavity due to the significant increase of pressure loss by approx. 60%, which can not be compensated by the slightly enhanced heat transfer of around 29%. Therefore, the thermo-hydraulic efficiency ranges between 0.808 and 1.105, depending on the applied definition. A quite contrary thermo-hydraulic efficiency can be achieved in case of the spherical dimple, which lies between 1.398 and 1.470. The reason for that impressive outcome is the moderate increase of pressure loss by almost 8%, which agrees with published results by Turnow et al. (2011), in comparison to the noticeable heat transfer augmentation of about 50%. Figure 5 depicts the time-averaged Nusselt number distribution at the clean lower channel wall with both structured surfaces, where regions of high convective heat transfer rates due to large velocity magnitudes and local vortex structures are primarily obtained within the surface structures and the downstream area behind the trailing edges. Especially the spherical dimple exhibits high Nusselt numbers of 100 and more over a relatively wide area, which explains the superior heat transfer enhancement compared to the square cavity.

The analysis of the thermo-hydraulic efficiency under consider-

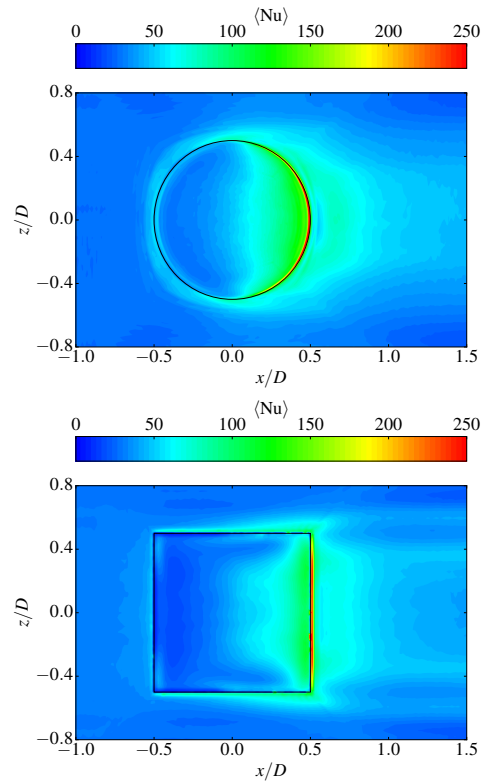


Figure 5. Time-averaged Nusselt number distribution at the clean lower channel wall for a spherical dimple (above) and a square cavity (below) at  $Re_D = 42000$

ation of foulant particle mass loading ratios up to  $\beta = 0.002$  are given in Table 2, which are less unambiguous as for the clean surfaces. The reason for this is the relatively small change of pressure loss and convective heat transfer, caused by the thin settled fouling layers after 120s of physical real time. Nevertheless, the present results provides a first trend concerning the fouling behavior of the investigated structured surfaces. According to this the square cavity seems to be more susceptible for fouling deposits, which leads to an increase of pressure loss of approx. 2% and a reduced heat transfer



by almost 0.5%. The spherical dimple shows only slightly changes in pressure loss and an almost stable convective heat transfer for all considered particle mass loading ratios  $\beta$ , which underlines the better fouling behavior in contrast to the cavity. Finally, Figure 6

Table 2. Thermo-hydraulic efficiency for different structured surfaces and mass loading ratios  $\beta$  after 120 s at  $Re_D = 42000$

	$\beta$	$C_f/C_{f0}$	$Nu/Nu_0$	$\frac{(Nu/Nu_0)}{(C_f/C_{f0})^{1/3}}$
Cavity	0.001	1.621	1.287	1.10
Dimple	0.001	1.075	1.505	1.47
Cavity	0.002	1.622	1.290	1.10
Dimple	0.002	1.083	1.508	1.47

illustrates the distribution and thickness  $h_f$  of the settled fouling layer for both structured surfaces after 120 s of simulated physical real time for an foulant particle mass ratio of  $\beta = 0.002$ . A relatively high amount of deposits with a total fouling layer height in the range of  $20\mu\text{m}$  and  $100\mu\text{m}$  can be observed within the recirculation zone of the spherical dimple in the vicinity of the leading edge, whereas no fouling is detected in the lee side of the dimple where the reattachment point of the flow lies. Additionally, comparable less fouling deposits are obtained at the channel wall downstream of the dimple trailing edge. The reason for this observation is probably the high wall shear stress in this particular regions due to the switching asymmetric vortex structures and vortex outbursts, because both extreme positions of the alternating vortex structures ( $\pm 45^\circ$ ) becomes faintly visible in the fouling and wall shear stress distribution (see Figure 7). Moreover, due to the flow acceleration in front of the dimple no fouling occurs in the area of the dimple front edge. In case of the square cavity, highest fouling deposition rates are obtained inside the forward half of the cavity, whereas the clean area downstream of the cavity trailing edge is significantly smaller compared to the spherical dimple.

## CONCLUSION

Time-resolved LES of the turbulent flow inside a smooth channel with a single spherical dimple or square cavity ( $t/D = 0.26$ ,  $Re_D = 42000$ ) and foulant particle mass loading ratios up to  $\beta = 0.002$  where performed and discloses the following major aspects:

1. Turbulent flow structures are of crucial importance for particulate fouling processes
2. The presence of unsteady asymmetric vortex structures inside the spherical dimple could be approved.
3. The clean spherical dimple shows a 37% higher thermo-hydraulic efficiency in comparison to the clean square cavity.
4. A considerable lower amount of fouling deposits in the periphery and inside of the spherical dimple due to the distinctive flow structures (improvement of the fouling mitigation ability).

These results confirms the necessity of large-scale resolving methods for extensive investigations of particulate fouling of structured heat transfer surfaces. Nevertheless, fouling simulations for larger time periods are necessary for a reasonable evaluation of the fouling performance. Notwithstanding the fact that the introduced phase conversion algorithm makes the fouling simulations very efficient, LES with hundred millions of particles (depending on the particle mass loading ratio) are very time consuming. Thus, a procedure

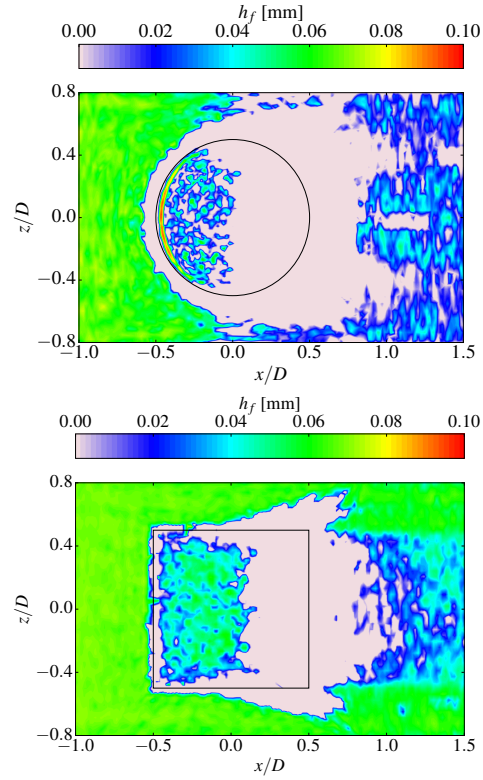


Figure 6. Distribution and height  $h_f$  of the settled fouling layer after 120 s of physical real time for an foulant particle mass loading ratio  $\beta = 0.002$  at  $Re_D = 42000$ : spherical dimple (above), square cavity (below)

for the extrapolation of the fouling layer will be introduced to prevent the enormous computational effort for huge fouling intervals. Additionally, experimental measurements are essential in order to validate our results and will be provided in the near future.

## ACKNOWLEDGMENT

The authors would like to thank the German Research Foundation (DFG, grant no. KO 3394/10-1 and INST 264/113-1 FUGG) and the North-German Supercomputing Alliance (HLRN) for supporting this work.

## REFERENCES

- Awad, M. M., 2011, Fouling of Heat Transfer Surfaces, Heat Transfer - Theoretical Analysis, Experimental Investigations and Industrial Systems, InTech.
- Bejan, A. and Kraus, A. D., 2003, Heat Transfer Handbook, John Wiley & Sons.
- Blöchl, R. and Müller-Steinhagen, H. M., 1990, Influence of Particle Size and Particle/Liquid Combination on Particulate Fouling in Heat Exchangers, Canadian Journal of Chemical Engineering, pp. 585-591.
- Chudnovsky, Y. and Kozlov, A., 2008, Experimental evaluation of heat transfer, pressure drop and fouling mitigation potential in finned, dimpled and bare tube bundles, Clean Air, Vol. 9, pp. 103-118.
- Crow, T. C., Schwarzkopf, J. D., Sommerfeld, M. and Tsuji, Y., 2011, Multiphase flows with droplets and particles, 2nd ed., CRC Press, Taylor & Francis.
- Elghobashi, S., 1994, On predicting particle-laden turbulent flows, Applied Scientific Research, Vol. 52, pp. 309-329.

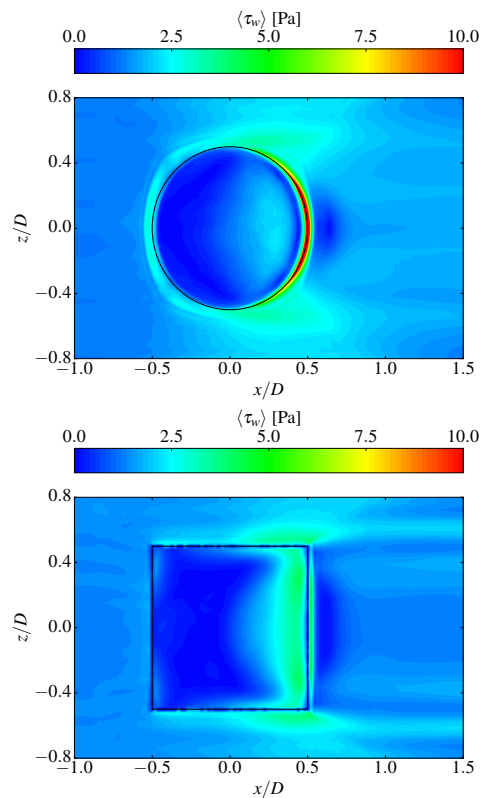


Figure 7. Time-averaged wall shear stress distribution at the clean lower channel wall for a spherical dimple (above) and a square cavity (below) at  $Re_D = 42000$

Elyyan, M. A., Rozati, A. and Tafti, D. K., 2008, Investigation of dimpled fins for heat transfer enhancement in compact heat exchangers, *Int. J. Heat Mass Transfer*, Vol. 51, pp. 2950-2966.

Epstein, N., 1988, *Fouling Science and Technology: Particulate Fouling*, NATO ASI Series, Vol. 145, pp. 143-164.

Gee, D. L. and Webb, R. L., 1980, Forced Convection Heat Transfer in Helically Rib-Roughened Tubes, *Int. J. of Heat Mass Transfer*, Vol. 23, pp. 1127-1136.

Germano, M., Piomelli, U., Moin, P. and Cabot, W. H., 1991, A dynamic subgrid-scale eddy viscosity model, *Phys. Fluids*, Vol. 3, pp. 1760-1765.

Heinl, E. and Bohnet, M., 2005, Calculation of particle-wall adhesion in horizontal gas-solids flow using CFD, *Powder Technol.*, Vol. 159, pp. 95-104.

Kern, D. Q. and Seaton, R. E., 1969, A Theoretical Analysis of Thermal Surface Fouling, *Brit. Chem. Eng.*, Vol. 4, pp. 258-162.

Kim, W. and Menon, S., 1995, A new dynamic one-equation subgrid-scale model for large eddy simulations, *AIAA, Aerospace Sciences Meeting and Exhibit*, 33 rd, Reno, NV.

Löffler, F. and Muhr, W., 1972, Die Abscheidung von Feststoffteilchen und Tropfen an Kreiszyindern infolge von Trägheitskräften, *Chemie-Ing.-Techn.*, Vol. 44, pp. 510-514.

Epstein, N., 1988, *Fouling Science and Technology: Particulate Fouling*, NATO ASI Series, Vol. 145, pp. 143-164.

Müller-Steinhagen, H. M., 2010, *Fouling of Heat Exchanger Surfaces*, VDI Heat Atlas, Springer.

Putnam, A., 1961, Integrable form of droplet drag coefficient, *ARS Journal*, Vol. 31, pp. 1467-1470.

Shah, R. K and Sekulić, D. P., 2003, *Fundamentals of Heat Exchanger Design*, John Wiley & Sons.

Sommerfeld, M., 2010, *Particle Motion in Fluids*, VDI Heat Atlas, Springer.

Taborek, J., Aoki, T., Ritter, R.B., Palen, J.W. and Knudsen, J.G., 1972, Predictive Methods for Fouling Behavior, *Chem. Eng. Prog.*, Vol. 68, pp. 69-78.

Talbot, L., Cheng, R. K., Schefer, R. W. and Willis, D. R., 1979, Thermophoresis of particles in a heated boundary layer, *J. Fluid Mech.*, Vol. 101, pp. 737-758.

Terekhov, V. I., Kalinina, S. V. and Mshvidobadse, Y. M., 1997, Heat transfer coefficient and aerodynamic resistance on a surface with a single dimple, *Journal of Enhanced Heat Transfer*, Vol. 4, pp. 131-145.

Turnow, J., Kornev, N., Isaev, S. and Hassel, E., 2011, Vortex mechanism of heat transfer enhancement in a channel with spherical and oval dimples, *Heat Mass Transfer*, Vol. 47, pp. 301-313.

Yoshizawa, A. and Horiuti, K., 1985, A statistically-derived subgrid-scale kinetic energy model for the large-eddy simulation of turbulent flows, *J. Phys. Soc. Jpn.*, Vol. 54, pp. 2834-2839.